Three-dimensional electromagnetic inversion of transfer function data from controlled sources

Rulff, Paula; Kalscheuer, Thomas; Bastani, Mehrdad; Zbinden, Dominik

DOI
10.1111/1365-2478.13660

Publication date
2024

Document Version
Final published version

Published in
Geophysical Prospecting

Received: 19 October 2023 | Accepted: 16 December 2024

DOI: 10.1111/1365-2478.13660

Geophysical Prospecting | EAGE EUROPEAN ASSOCIATION OF GEOSCIENTISTS & ENGINEERS

ORIGINAL ARTICLE

Three-dimensional electromagnetic inversion of transfer function data from controlled sources

Paula Rulff[1,2] | **Thomas Kalscheuer**[1] | **Mehrdad Bastani**[1,3] | **Dominik Zbinden**[1]

[1]Department of Earth Sciences, Uppsala University, Uppsala, Sweden

[2]Department of Geoscience and Engineering, TU Delft, Delft, The Netherlands

[3]Geological Survey of Sweden, Uppsala, Sweden

Correspondence
Paula Rulff, Department of Geoscience and Engineering, TU Delft, Stevinweg 1, Delft, CN, 2628, The Netherlands.
Email: p.rulff@tudelft.nl

Funding information
Smart Exploration project; European Union's Horizon 2020, Grant/Award Number: No. 775971; National Academic Infrastructure for Supercomputing in Sweden (NAISS), Grant/Award Number: Dnr: SNIC 2022/5-530

Abstract

We develop a three-dimensional inversion code to image the resistivity distribution of the subsurface from frequency-domain controlled-source electromagnetic data. Controlled-source electromagnetic investigations play an important role in many different geophysical prospecting applications. To evaluate controlled-source electromagnetic data collected with complex measurement setups, advanced three-dimensional modelling and inversion tools are required.

We adopt a preconditioned non-linear conjugate gradient algorithm to enable three-dimensional inversion of impedance tensor and vertical magnetic transfer function data produced by multiple sets of two independent active sources. Forward simulations are performed with a finite-element solver. Increased sensitivities at source locations can optionally be counteracted with a weighting function in the regularization term to reduce source-related anomalies in the resistivity model. We investigate the capabilities of the inversion code using one synthetic and one field example. The results demonstrate that we can produce reliable subsurface models, although data sets from single pairs of independent sources remain challenging.

KEYWORDS
electromagnetics, imaging, inversion, resistivity

INTRODUCTION

Frequency-domain controlled-source electromagnetic (CSEM) techniques aim at investigating the subsurface resistivity distribution using artificial electric or magnetic sources transmitting signals at distinct frequencies. While data acquisition and evaluation methods for marine CSEM are well established, the interest in conducting land-based CSEM surveys has increased during the last decade (e.g. Castillo-Reyes et al., 2021; Grayver et al., 2014; Kalscheuer et al., 2015; Pedersen et al., 2005; Streich, 2016; Schaller et al., 2018; Tietze et al., 2019). However, it is challenging to obtain reliable subsurface resistivity images from land-based CSEM setups for a number of reasons: First, the receiver coverage is often less dense and less uniform compared to marine or airborne CSEM settings and, therefore, the sensitivity distribution can vary by orders of magnitude in the area of interest and subsurface resistivity anomalies are more difficult to resolve (Avdeev & Avdeeva, 2009). Second, the number of transmitter positions is often limited due to logistical reasons (Grayver et al., 2014), resulting in an unsymmetrical illumination of the target (Bretaudeau & Coppo, 2016). Third, for electric sources, shallow inhomogeneities at the transmitter site can lead to considerable source

overprint (Commer & Newman, 2008; Hördt & Scholl, 2004; Kalscheuer et al., 2015; Zonge & Hughes, 1991).

Several three-dimensional (3D) frequency-domain CSEM inversion codes have been developed in the last two decades and are frequently used in the scientific electromagnetic (EM) community (Abubakar et al., 2009; Bretaudeau & Coppo, 2016; Cai et al., 2021; Cao et al., 2016; Commer & Newman, 2008; Gribenko & Zhdanov, 2007; Grayver et al., 2013; Heagy et al., 2017; Haber et al., 2004; Kelbert et al., 2014; Long et al., 2020; Mackie et al., 2007; Newman & Boggs, 2004; Plessix & Mulder, 2008; Rochlitz et al., 2023; Smirnova et al., 2023; Zhang, 2015). Among these, the most popular approach for solving the EM non-linear inverse problem is to use the Gauss–Newton minimization technique in combination with a direct forward solver (Bretaudeau and Coppo, 2016; Cai et al., 2021; Grayver et al., 2013; Kara & Farquharson, 2023; Long et al., 2020; Rochlitz et al., 2023). Non-linear conjugate gradient (NLCG) techniques in combination with iterative forward solvers are the second method of choice (Commer & Newman, 2008; Kelbert et al., 2014; Newman & Boggs, 2004). NLCG methods exhibit poorer convergence rates than Gauss–Newton methods (Amaya, 2015), but model updates in each iteration are less computationally expensive, as only gradient vectors rather than full Jacobian matrices need to be computed to obtain the relevant first-derivative information.

No matter which of the above-mentioned inversion approaches is applied, the sensitivity or gradient patterns guide the inverse algorithms, such that model updates are performed more likely in model cells with high sensitivities. For CSEM problems, gradient dynamics are high around the sources and receivers (Grayver et al., 2014). Sensitivities towards the specific investigation targets can be enhanced with customized measurement setups (Streich, 2016). However, in land-based CSEM surveys often the deep resistivity distribution of the subsurface is to be investigated, while data sets are generated with only a few transmitters (Bretaudeau & Coppo, 2016). Thus, the convergence behaviour might be deteriorated by sensitivity patterns related to the source footprint throughout the model. High absolute values of the data gradients, which can appear in natural and controlled-source EM applications, for example in the vicinity of the receiver sites, can produce artefacts in the model (Avdeev & Avdeeva, 2009).

To achieve reliable inversion results of CSEM data with complicated sensitivity patterns, some approaches counteracting the sensitivity heterogeneities have been suggested: Grayver et al. (2013) use a preconditioner based on Jacobi diagonal scaling, which aims at preventing large updates near sources and receivers and thus distributing the model update more evenly in the model domain compared to unpreconditioned updates. Bretaudeau and Coppo (2016) state that the influence of increased sensitivity at the transmitter is reduced by using CSEM data in the form of impedances generated by two source polarizations. However, Sasaki et al. (2015) observe that the inversion of electric and magnetic fields obtained with a single source polarization results in better convergence and yields a better resistivity model compared to the inversion of scalar apparent resistivities and phases. To compensate for the sensitivity loss with depth, Plessix and Mulder (2008) investigate a reparameterization approach called 'model depth weighting'. They apply a linear operator that includes amplitude decay and geometrical spreading factors to the model parameters. To account for the large amplitude decay at high frequencies for large source–receiver offsets, Plessix and Mulder (2008) additionally use a heuristic data weighting functional. Avdeev and Avdeeva (2009) suggest an additional model regularization to counteract the gradient pattern at the receiver sites in magnetotelluric inversion. Their approach is based on smoothing the gradients of the objective function in the vicinity of gradient singularities in the continuous formulation of the EM problem. For airborne CSEM setups, Rochlitz et al. (2023) find that the use of second-order basis functions for EM field simulation, which improves the accuracy of the forward responses for the weaker field components, can avoid artefacts in the vicinity of transmitters or at the surface.

Following Bretaudeau and Coppo (2016) and Smirnova et al. (2023), we invert transfer functions in the form of impedance tensor components and, additionally, vertical magnetic transfer functions (VMTF), a method also called controlled-source-tensor magnetotellurics (e.g. X. Li & Pedersen, 1991, cf. Section Methods 2). This method is not standard for 3D CSEM inversion. Often, EM field components normalized by the recorded source currents are used as input data (e.g. Grayver et al., 2013; Kelbert et al., 2014; Kara & Farquharson, 2023; Rochlitz et al., 2023; Zhang, 2015). However, we have found that inverting impedance tensors and vertical magnetic transfer functions instead of EM field components can be beneficial for efficiently recovering the overall resistivity distribution below the stations by reducing the footprints of the sources (Rulff & Kalscheuer, 2024).

Our inversion workflow includes a 3D finite-element forward modelling routine (Rulff et al., 2021, cf. Section The Forward Algorithm) and is based on a preconditioned NLCG algorithm (Zbinden, 2015, cf. Section The Non-Linear Conjugate Gradients Inverse Algorithm). Conjugate gradient techniques rely on computing optimal search directions that are conjugate to each other. However, when solving the non-linear EM inverse problem with an NLCG algorithm, the search directions can loose conjugacy, which deteriorates its convergence properties (Shewchuk, 1994). A preconditioner, previously tested by Newman and Alumbaugh (2000) and Newman and Boggs (2004) for magnetotelluric inversion, is constructed to improve the convergence of our CSEM inversion (cf. Section Preconditioning). We propose options

for model regularization, which aim at counteracting high sensitivity near source locations in 3D CSEM inversion. Following Avdeev and Avdeeva (2009), our focus is on model regularization because we consider the model regularization term as the adequate part of the EM inverse problem to constrain the inversion and to provide prior information for guiding the model to a preferred direction. Thus, we formulate a distance weighting functional (cf. Section Distance-to-Source Weighting) applied to the regularization term that increases the smoothing in regions close to the sources to obstruct the production of artefacts there. The proposed regularization technique is investigated for a synthetic model (cf. Section Synthetic Data Example). Additionally, we demonstrate the inversion of CSEM field data collected on a frozen lake (cf. Section Application to Field Data).

METHODS

The discrete non-linear inverse problem is formulated as a minimization of the objective function Φ that consists of two terms: a weighted difference between observed and predicted data (Φ_d) and a regularization term (Φ_m):

$$\begin{aligned}\Phi(\mathbf{m}) &= \Phi_d(\mathbf{m}) + \lambda\Phi_m(\mathbf{m}) \\ &= (\mathbf{d}^{\text{obs}} - \mathbf{F}(\mathbf{m}))^T \mathbf{C_d}^{-1}(\mathbf{d}^{\text{obs}} - \mathbf{F}(\mathbf{m})) \\ &\quad + \lambda(\mathbf{m} - \mathbf{m}_{ref})^T \mathbf{C_m}^{-1}(\mathbf{m} - \mathbf{m}_{ref}).\end{aligned} \tag{1}$$

Here, $\mathbf{d}^{\text{obs}}$ are the observed input data and $\mathbf{F}(\mathbf{m})$ is the data vector obtained through forward modelling of the model $\mathbf{m}$ containing $[M]$ elements (number of model parameters). Vectors $\mathbf{d}^{\text{obs}}$ and $\mathbf{F}(\mathbf{m})$ have $[N]$ elements (number of data). $\mathbf{C_d} = \text{diag}(\epsilon_n^2)$ denotes the data covariance matrix holding the data uncertainty ϵ_n for each data item n. $\mathbf{C_m}$ is the model covariance matrix, $\mathbf{m}_{ref}$ is a vector holding optional reference model parameters and T stands for the transposition operator. λ controls the strength of the model regularization and is kept constant during the non-linear conjugate gradient (NLCG) inversion. In this article, we express λ in $\log_{10}$-values.

Input data for the inversion are complex transfer functions, that is the impedance tensor $\mathbf{Z}$ and the vertical magnetic transfer function (VMTF) tensor $\mathbf{T}$

$$\mathbf{Z} = \begin{pmatrix} Z_{xx} & Z_{xy} \\ Z_{yx} & Z_{yy} \end{pmatrix} \quad \text{and} \quad \mathbf{T} = \begin{pmatrix} \mathrm{T}_x & \mathrm{T}_y \end{pmatrix}, \tag{2}$$

generated by a set of two approximately perpendicularly oriented horizontal electric or horizontal magnetic dipole or bipole sources, also known as 'tensor controlled-source audio-magnetotellurics' (Smirnova et al., 2023; Zonge & Hughes, 1991), 'pseudo-MT tensor formulation' (Bretaudeau & Coppo, 2016) or 'controlled-source tensor magnetotellurics' (Cao et al., 2016; X. Li & Pedersen, 1991). The subscripts x, y, z in Equation (2) describe the Cartesian coordinate directions. The individual components of $\mathbf{Z}$ and $\mathbf{T}$ are defined via the horizontal electric and horizontal and vertical magnetic field components E_{x1}, E_{y1}, H_{x1}, H_{y1}, H_{z1} and E_{x2}, E_{y2}, H_{x2}, H_{y2}, H_{z2} aligned in x-, y- or z-directions and obtained with two independent source polarizations (subscripts 1 and 2) as

$$\begin{aligned} Z_{xx} &= \frac{E_{x1}H_{y2} - E_{x2}H_{y1}}{H_{x1}H_{y2} - H_{x2}H_{y1}}, & Z_{xy} &= \frac{E_{x2}H_{x1} - E_{x1}H_{x2}}{H_{x1}H_{y2} - H_{x2}H_{y1}}, \\ Z_{yx} &= \frac{E_{y1}H_{y2} - E_{y2}H_{y1}}{H_{x1}H_{y2} - H_{x2}H_{y1}}, & Z_{yy} &= \frac{E_{y2}H_{x1} - E_{y1}H_{x2}}{H_{x1}H_{y2} - H_{x2}H_{y1}}, \\ \mathrm{T}_x &= \frac{H_{z1}H_{y2} - H_{z2}H_{y1}}{H_{x1}H_{y2} - H_{x2}H_{y1}}, & \mathrm{T}_y &= \frac{H_{z2}H_{x1} - H_{z1}H_{x2}}{H_{x1}H_{y2} - H_{x2}H_{y1}}. \end{aligned} \tag{3}$$

No data transformation is applied. As the actual source current strengths (both amplitude and phase) cancel out in this formulation, they do not have to be known for the inversion. However, the transfer functions are generally dependent on source location and geometry.

We aim to fit our data within the ranges of the data uncertainties ϵ_n, defined by the noise level or error floor. Thus, the root mean square error (RMS) is used as a measure for the total data misfit:

$$\text{RMS} = \sqrt{\frac{1}{N}\sum_{n=1}^{N}\left(\frac{d_n^{\text{obs}} - F_n(\mathbf{m})}{\epsilon_n}\right)^2}. \tag{4}$$

In accordance with Pedersen (1982), the real and imaginary parts of the impedance tensor or VMTF components are assigned the same uncertainties. For the synthetic examples presented in the following, the off-diagonal impedance tensor components are given amplitude-dependent uncertainties, for example $\epsilon_{Zxy} = |Zxy|\ \epsilon^r$, where ϵ^r is a predefined relative error floor. The values of the diagonal components of the impedance tensors are overall approximately one decade smaller than the off-diagonal components. Therefore, the use of relative error floors of the same percentage as for the off-diagonal components would bias the weights of the data points in the inversion towards the smaller diagonal components. A typical assumption for impedance tensor estimation is, that only the electric field is contaminated with noise (Pedersen, 1982). Hence, we allow for correlation between the uncertainties of the impedance tensor components in the same row of the impedance tensor by setting the uncertainties of the diagonal components to the maximum

uncertainties of the corresponding rows of $\mathbf{Z}$, for example $\epsilon_{Zxx} = \max(|Zxx|\ \epsilon^r, |Zxy|\ \epsilon^r)$. Except for in the extreme near-field zone, the VMTF amplitudes vary smoothly in a range between $+/-1$. To reduce the weight of close-to-zero VMTF data points in the inversion, frequency-independent absolute uncertainties are assigned to the VMTF components.

The forward algorithm

To perform the forward simulations, that is to calculate the predicted data $\mathbf{F}(\mathbf{m})$, in the inversion procedure, 3D finite-element (FE) routines (Rulff et al., 2021) are implemented into the inversion framework `emilia` (cf. the Appendix and Figure A.1). The code uses the total-field formulation in terms of the electric field combined with edge-based linear vector Nédélec interpolation functions. Note that a total-field approach for inverse modelling is rarely used (Rochlitz et al., 2023, and references therein), but we favour the straight-forward implementation of extended sources along element edges in the total-field forward modelling approach and want to investigate its suitability as a forward solver in inverse modelling. The code simulates frequency-domain 3D controlled-source electromagnetic (CSEM) setups for electric and magnetic sources on tetrahedral meshes using a direct forward solver, currently `MUMPS` (Amestoy et al., 2016), for the linear system of equations $\mathbf{AE} = \mathbf{b}$.

The system is solved for the unknown electric field values stored in vector $\mathbf{E}$. The right-hand side vector $\mathbf{b}$ contains the source information, while the system matrix $\mathbf{A}$ contains information about the material parameters within the discretized computational domain. Homogeneous Dirichlet boundary conditions for the electric field are applied. The forward modelling routine calculates responses (electric and magnetic fields in Cartesian coordinates) for multiple sources as well as the resulting transfer functions, that is impedances and VMTF, which serve as forward data $\mathbf{F}(\mathbf{m})$ during inversion.

The non-linear conjugate gradients inverse algorithm

The NLCG algorithm was initially implemented into the inversion framework `emilia` (cf. Appendix and Figure A.1) for solving two-dimensional (Radi-o) Magnetotelluric ((R-)MT) inverse problems (Zbinden, 2015). However, due to the object-oriented modular structure of `emilia`, the NLGC implementation is independent of the type of data, the dimension of the model and the discretization method. To enable 3D CSEM inversion, not only a 3D CSEM forward code (cf. Section The Forward Algorithm) but also new modules for CSEM data handling, data gradient computations and model regularization for tetrahedral meshes are designed. The data module can handle data and data uncertainties originating from an arbitrary station distribution and multiple transmitter locations. For the data gradient computations, the system matrix of the FE forward computations is re-used for solving the ensuing pseudo-forward problems. In the regularization module, the model covariance matrix is computed and stored in a sparse format by taking a specific model regularization option (cf. Section Regularization) and the geometric relations between the tetrahedral elements comprising the model parameters for inversion into account.

Material parameters included in the forward modelling process are cell-wise constant electrical resistivities, magnetic permeabilities and dielectric permittivities defined on a tetrahedral FE mesh generated with the open-source mesh generator `Tetgen` (Si, 2015). The mesh fulfils the basic requirements for accurate forward responses, such as small, well-shaped elements in the vicinity of receivers and sources and padding cells towards the domain boundaries. The inverse algorithm inverts for electrical resistivities within an inner subset of the forward mesh, which we refer to as the set of model parameters hereinafter. To prevent artefacts, model parameters in the immediate vicinity of the sources can be fixed during the inversion (Grayver et al., 2013). During the inversion procedure, the algorithm updates the model parameters in order to fit the observed data. To prevent the inversion from producing negative or unrealistically high or low resistivity values, we apply a logarithmic model parameter transformation using bounds for lower and upper resistivities (e.g. Commer & Newman, 2008; Grayver et al., 2013; Kim & Kim, 2011).

For minimizing the objective function (Equation 1), we follow the basic preconditioned NLCG approach (e.g. Fletcher & Reeves, 1964; Nocedal & Wright, 2006; Newman & Alumbaugh, 2000; Newman & Boggs, 2004; Newman & Commer, 2008). In the NLCG algorithm, the factor for correcting the search direction away from the steepest descent direction is calculated as suggested by Polak and Ribiere (1969).

Gradients of the objective function (Equation 1) with respect to (w.r.t.) the model parameters $\mathbf{m}$, that is

$$\begin{aligned}\nabla\Phi(\mathbf{m}) &= \nabla\Phi_d(\mathbf{m}) + \lambda\nabla\Phi_m(\mathbf{m}) \\ &\approx -2\mathbf{J}^T{\mathbf{C_d}}^{-1}(\mathbf{d}^{\text{obs}} - \mathbf{F}(\mathbf{m})) + 2\lambda{\mathbf{C_m}}^{-1}\mathbf{m},\end{aligned} \tag{5}$$

have to be computed to define the search direction $\mathbf{u}_k$. Here, $\mathbf{J}$ is the sensitivity matrix (Jacobian) containing the partial derivatives of all data (index n) w.r.t. all model parameters (index i). The sensitivity matrix connects changes in the model vector to changes in the forward modelled data vector. We obtain the gradients as described in Newman and Alumbaugh (2000) without explicit calculation of the Jacobian. We use a real-valued formulation of the optimization problem that is equivalent to computing the $\nabla\Phi_d$ functional

for complex-valued data and forward responses ($N = 2N_c$) via matrix-vector products as

$$\nabla\Phi_d(\mathbf{m}) = \frac{\partial\Phi_d}{\partial m_i} = 2\,\mathrm{Re}\left[\sum_{n=1}^{N_c}(\Delta d_n)^{*1}\boldsymbol{\gamma}_n^T\mathbf{A}^{-1}\left(\frac{\partial\mathbf{A}}{\partial m_i}\mathbf{E}_1\right) + \sum_{n=1}^{N_c}(\Delta d_n)^{*2}\boldsymbol{\gamma}_n^T\mathbf{A}^{-1}\left(\frac{\partial\mathbf{A}}{\partial m_i}\mathbf{E}_2\right)\right]. \quad (6)$$

This results in a set of additional pseudo-forward problems per frequency. Here, $\mathbf{A}$ is the system matrix and $\mathbf{E}_1$ and $\mathbf{E}_2$ are the electric field vectors for two source polarizations. $(\Delta d_n)^*$ is the complex conjugate of the weighted data difference $(d_n^{\mathrm{obs}} - F_n(\mathbf{m}))/\epsilon_n^2$ formulated in terms of complex impedance or VMTF tensor components Z_n or T_n. ${}^{1,2}\boldsymbol{\gamma}_n^T$ are linear combinations of vectors (Newman & Alumbaugh, 2000), which interpolates the fields for the two source polarizations from the forward modelling mesh to the receiver sites. We checked the data gradients $\nabla\Phi_d$ for consistency by comparing them to cell-wise gradients calculated with the perturbation method (McGillivray & Oldenburg, 1990). Compared to $\nabla\Phi_d$, the $\nabla\Phi_m$ functional is inexpensive to obtain.

Preconditioning

The convergence of the NLCG algorithm is accelerated with a preconditioner $\mathbf{M}$ to obtain a favourable search direction. The preconditioner aims at approximating the second derivative, that is the Hessian, of the objective function (Shewchuk, 1994). We implemented the time- and memory-efficient diagonal preconditioner suggested by Newman and Alumbaugh (2000). Updated at each iteration, this formulation of a preconditioner does not need any additional computations because all required terms are already obtained within the NLCG scheme. The search direction is ensured to be a descent direction by not updating a particular diagonal entry of $\mathbf{M}$ in case it would be negative. Newman and Alumbaugh (2000) set the start preconditioner $\mathbf{M}_0$ to the identity matrix, which results in good convergence behaviour for the models shown in this article.

However, the identity matrix is a very poor approximation of the Hessian. Therefore, it might hinder inversions to converge in some cases (Zbinden, 2015). To obtain a better search direction from the start, Jacobi-diagonal scaling for the start preconditioner, that is

$$\mathbf{M}_0 = \mathrm{diag}\left(2\mathbf{J}^T\mathbf{C_d}^{-1}\mathbf{J} + 2\lambda\mathbf{C_m}^{-1}\right), \quad (7)$$

is also implemented. As a result, the preconditioner $\mathbf{M}$ is closer to the approximate Hessian in the first iterations. The disadvantage is that we have to evaluate the full Jacobian once at the beginning of an inversion, which is time and memory consuming. The preconditioned search direction is then defined by left-multiplying the gradient of the objective function by the inverse of $\mathbf{M}$.

Regularization

The regularization term Φ_m (Equation 1) constrains the inverse problem through introducing smoothing (Tikhonov & Arsenin, 1977) into the model. The inverse model covariance matrix $\mathbf{C_m}^{-1}$ can be described in terms of a product $\mathbf{L}^T\mathbf{L}$, which we implement as a first-order difference operator (Günther et al., 2006) and a model parameter gradient approximation via the weighted sum of first differences (Key, 2016). No reference model is used (Equation 1). Prior to the inversion, we define weights of the element-to-element regularization operators to allow for more roughness in model regions, where more abrupt resistivity variations are expected, and to increase the smoothing in model regions, where sensitivities are high, but no variations in subsurface resistivity are expected. These structural weights on the regularization operator are implemented as a diagonal weighting matrix $\mathbf{w} = \mathrm{diag}(w_s)$ for $s = 1, \ldots, S$ (Rücker, 2011) multiplied from the left to the regularization matrix $\mathbf{L}$. S is the total number of individual structural constraints, that is of inner model faces between elements. In this manner, weights at interfaces between different pre-defined model regions can be reduced, allowing to incorporate the information on boundaries between lithological units obtained with, for example borehole measurements or seismic methods. In this case, the inversion mesh has to be designed in a way that inner faces are aligned with the boundaries between units, where the smoothing shall be reduced. Structural anisotropic constraints can also be included via the diagonal weighting matrix $\mathbf{w}$ (Rücker, 2011) for first-order differences or via a weighted distance measure (Key, 2016) for the gradient approximation. For instance, if a layered subsurface is expected, lower weights for smoothing across horizontal compared to vertical boundaries can be imposed.

Distance-to-source weighting

The distance-to-source weighting is a more advanced type of structurally weighting the regularization operator. It is based on the concept of depth weighting that has been introduced for the regularization of 3D magnetic and gravity inverse problems (Kamm et al., 2015; Y. Li & Oldenburg, 1993) in order to distribute the model update more evenly in the domain and to counteract the effects of high sensitivity near

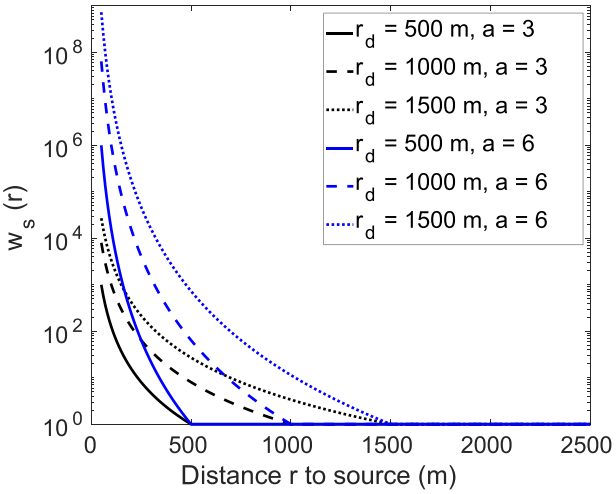

FIGURE 1 Distance-to-source weighting function $w_s(r)$, Equation (8): weights with increasing distance r to source for different distance thresholds r_d and exponents a.

the surface. Plessix and Mulder (2008) apply a heuristic depth weighting function to model parameter transformation explicitly for CSEM inversion. We have tested a set of different weighting functions including depth and distance-to-source weightings to prevent resistivity artefacts close to the source location. Such artefacts can arise in models, where the sensitivity distribution is very heterogeneous due to using only one source location. Of the approaches we have tested, the following function, which only includes a distance-to-source weighting, results in the most reliable models while being mathematically simple:

$$w_s(r) = \begin{cases} \left(\frac{r_d}{r}\right)^a & \text{for} \quad r \le r_d \\ 1 & \text{for} \quad r > r_d \end{cases}, \tag{8}$$

where r is the distance between the centre of boundary face s and the source midpoint or the closest source electrode. Exponent a is supposed to be a small positive integer and can be chosen by the user, depending on how much the smoothing shall be increased in the source region. Threshold r_d describes until which distance from the source the model smoothing remains increased. It has to be chosen smaller than the distance between the source and expected anomalies in the subsurface. Distance r_d influences not only the size of the area with increased smoothing but also the maximum smoothing at the source, that is the steepness of the function $w_s(r)$ (cf. Figure 1). The minimum of the function, that is the most reduction in smoothing, is reached at $r = r_d$ and stays constant for $r > r_d$. As the weights in the regularization operator are evaluated at the midpoints of element interfaces, r never gets zero and we avoid singularities at the source that is implemented on element edges.

SYNTHETIC DATA EXAMPLE

For demonstrating the inversion for a realistic source–receiver setting with a single source location, we use a controlled-source electromagnetic (CSEM) field setup above a mineral deposit in central Sweden with a simplified anomaly geometry. The model includes one anomalous object (Figure 2) that simulates an iron ore deposit located in the Bergslagen region in central Sweden. The physical properties, sizes and shapes of the real deposit as well as its host rock have been extensively studied with geophysical measurements in recent years (Bastani et al., 2019, 2020; Maries et al., 2017; Malehmir et al., 2017; Markovic et al., 2020). We chose the presented measurement setup (Figure 2a) because test measurements were performed at the corresponding field site with a similar source–receiver layout. Due to logistical reasons, we were limited to one source location. A detectability study determining favourable station locations and frequencies where the signal would be sensitive to the mineral deposits had been conducted before the test measurements took place (Rulff et al., 2021). Due to malfunctioning sensors, the data of the test measurements are faulty and cannot be evaluated. However, using the synthetic model (Figure 2), we investigate whether the developed inversion algorithm can detect the location and resistivity of the geometrically simplified mineral deposit. Resistivities of 500 and 10,000 Ωm are assigned to the mineral deposit and a surrounding half-space, respectively. The air half-space is modelled with a resistivity of 10^8 Ωm. Simulated data for the true model are generated on a high-quality tetrahedral mesh (836,235 elements, 969,722 degrees of freedom). The overall domain size amounts to 60×60×60 km.

The input data for inversion are impedance and vertical magnetic transfer function (VMTF) tensor components at 16 distributed receiver stations (for locations, see Figure 2a). An L-shaped pair of two long grounded cables located south-west of the receiver stations serves as sources transmitting currents in two orthogonal directions at 11 frequencies between 100 and 10,000 Hz. This setting results in a total number of 1056 complex data points. Normally distributed random noise of 2% is added to the impedance data. Consequently, a relative error floor of 2% is used to determine data uncertainties (Section Methods). The VMTF components are contaminated with an absolute noise level of 0.02, and their absolute uncertainties are set accordingly, which corresponds to a minimum relative error floor of 2% considering that maximum VMTF amplitudes are $+/-1$ (cf. Figure 3).

The inversion mesh is decoupled from the mesh used to generate the synthetic input data for the inversion, that is we use coarser refinement at receivers, do not incorporate the anomaly shapes in the mesh and use a lower mesh quality. A homogeneous half-space of 10,000 Ωm corresponding to

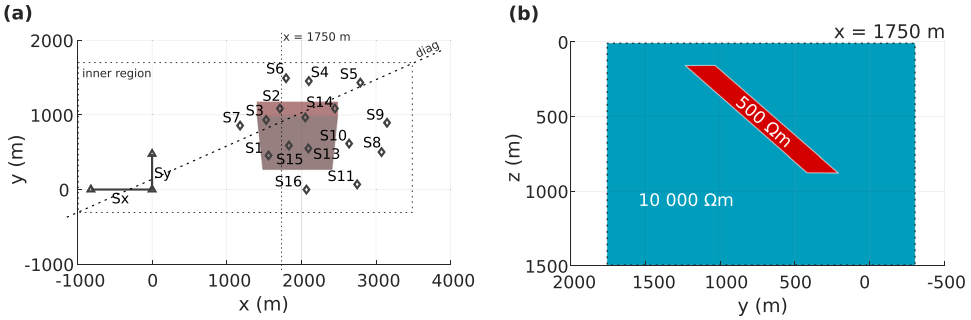

FIGURE 2 Synthetic example: (a) Top view on measurement setup with locations of the inclined block anomaly representing the mineral deposit (red feature) in a local coordinate system. The locations of the source electrodes (Sx, Sy) and of the 16 receiver stations (S1–S16) at the surface are marked with triangle and diamond symbols, respectively. (b) Vertical section through the inner model region displays the true model resistivities.

the known approximate resistivity of the host rock (Maries et al., 2017) is used as a start model. To prevent model updates in the cells hosting the extended bipole sources, a thin layer with the host rock resistivity is fixed right below the surface. We observed that this is not essential, but it can result in better convergence of the inversion (Rulff, 2023). Below, the inner part of the inversion mesh containing the free model parameter cells is rather uniformly discretized and comprises only the central model region. This results in 67,663 free model parameters within the inner model region. The gradient approximation is used for model regularization. An optimal regularization parameter $\lambda = 6.0$ is found to give the combination of the smoothest model and the smallest root mean square error (RMS) after running the inversion with a set of different λ for 30 iterations.

Sensitivities

In order to assess the sensitivity distribution of the data, we investigate the normalized data gradient pattern, that is $\mathbf{J}^T\mathbf{C_d}^{-1}(\mathbf{d}^{\text{obs}} - \mathbf{F}(\mathbf{m}))$, called *data gradients* hereinafter, for the homogeneous start model of 10,000 Ωm (cf. Figure 4) using the full data set. The data gradients show sensitivity concentrations below the source and underneath the station array. At the endpoints of the source bipoles, polarity changes in the gradients can be observed. Strong negative gradients at the location of the anomaly (outlined in white) indicate that the data are sensitive to the conductive mineral deposit. Through comparison of the input data for the inversion to the data produced by the homogeneous half-space start model (Figure 3), one can observe significant differences between both. This also indicates that the data are sensitive to the anomalous structure. We aim at counteracting the elevated sensitivity levels in the vicinity of the source by testing the proposed distance-to-source weighting in the regularization term (cf. Section Distance-to-Source Weighting).

Analysis of inversion properties

Inversion parameter tests were performed. The following four test inversions (cf. Figure 5a–d), which examine the modified start preconditioner (cf. Section Preconditioning) and the newly implemented distance-to-source weighting options (cf. Section Distance-to-Source Weighting), are potentially of interest to the research community:

(a) A non-weighted gradient approximation regularization operator is used.
(b) A non-weighted gradient approximation regularization operator and Jacobi diagonal scaling for the start preconditioner (cf. Equation 7) are used.
(c) A gradient approximation regularization operator with distance-to-source weighting, a threshold $r_d = 750$ m and an exponent $a = 3$ (Equation 8) are used.
(d) A gradient approximation regularization operator with distance-to-source weighting, a threshold $r_d = 750$ m and an exponent $a = 6$ (Equation 8) are used.

Each inversion was run for 30 iterations.

Modified start preconditioner (b): Applying Jacobi-diagonal scaling for the start preconditioner (Equation 7) is computationally expensive, that is inversion (b) requires approximately twice as much time as inversion (a). On the other hand, the modified start preconditioner improves the convergence rate of the inversion in the earlier iterations, that is in inversion (b) an RMS of 1.1 is already reached after 20 iterations compared to 29 iterations in inversion (a). However, using the Jacobi-diagonal scaling in the start preconditioner, elevated sensitivity levels at the surface and the source location (Figure 4) are translated to distinct conductive and resistive artefacts (Figure 5b). Therefore, we cannot recommend to the use of the Jacobi-diagonal scaling in the start preconditioner for CSEM applications with sensitivity patterns produced by a single source location.

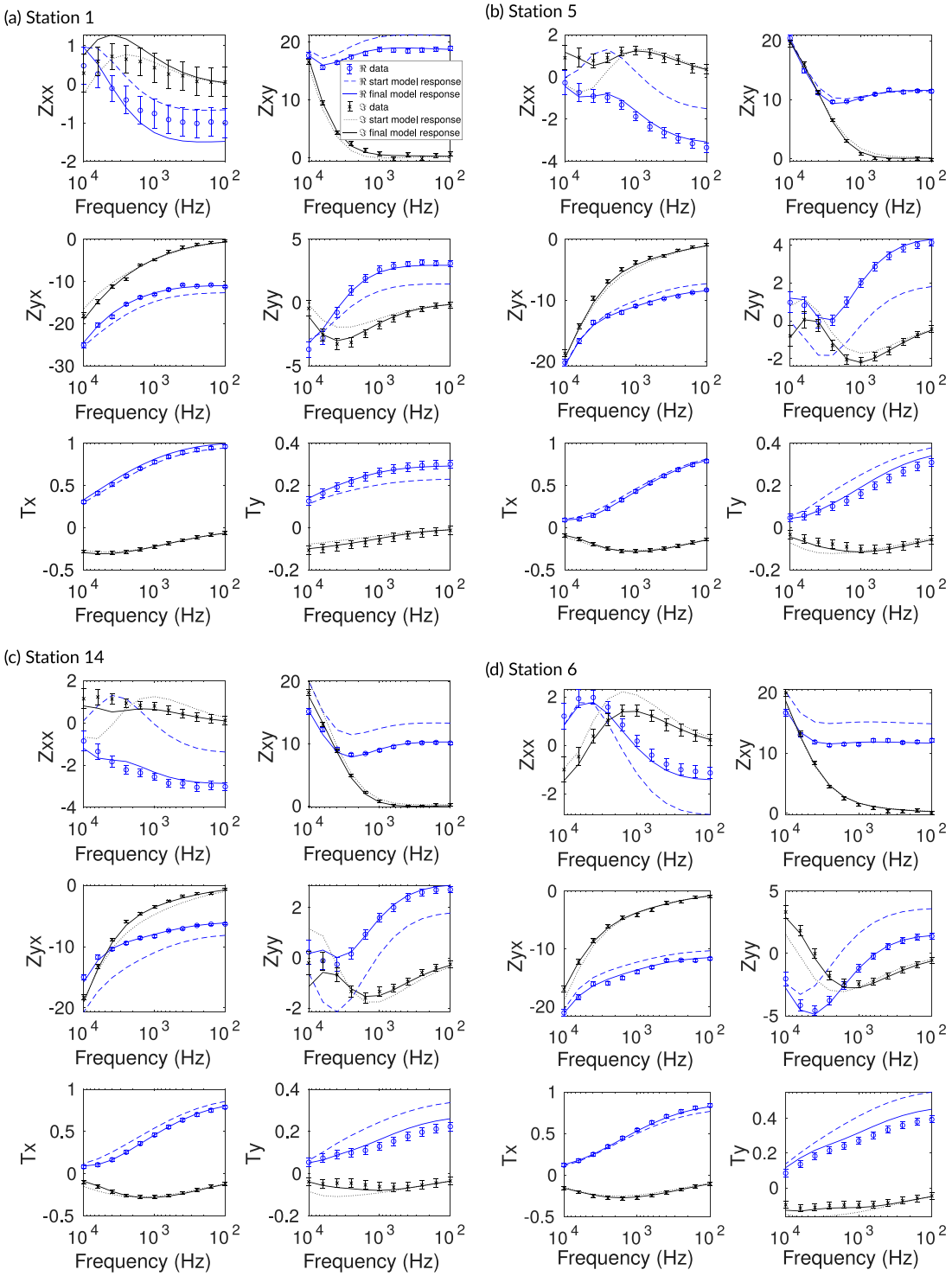

FIGURE 3 Synthetic example: real (blue symbols) and imaginary (black symbols) components of synthetic transfer functions with uncertainties. Dashed and solid lines represent forward responses of the start model and the final inversion model (cf. Figures 5d and 7) produced with distance-to-source weighting ($a = 6$, $r_d = 750$ m), respectively. The displayed data of stations 1, 5, 6 and 14 are representative of the overall data fit (cf. Figure 6). The average RMS is 1.1. The legend in (a) is valid for all sub-figures.

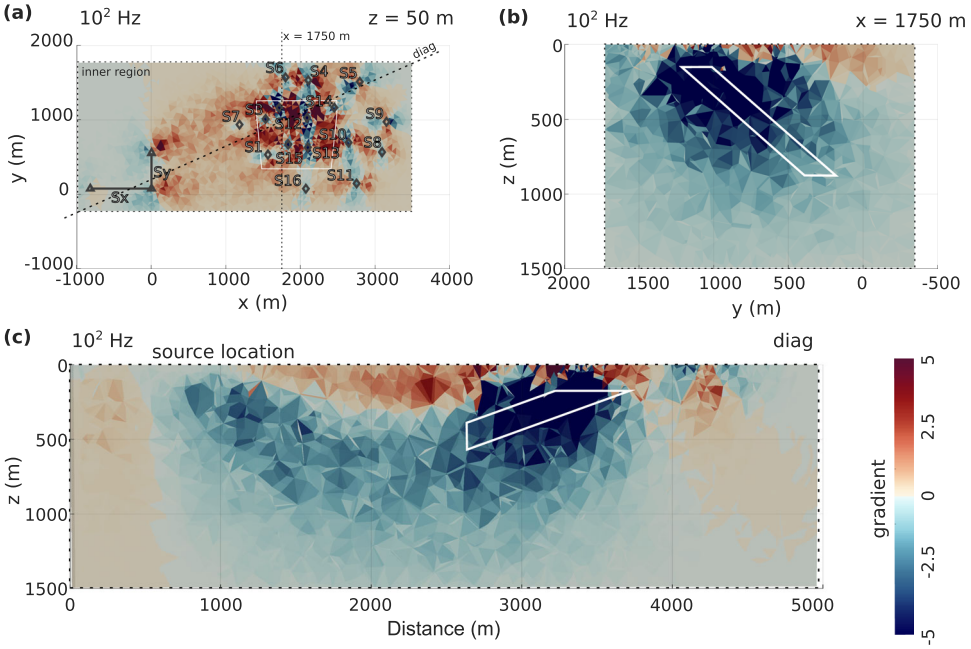

FIGURE 4 Synthetic example: (a) Horizontal and (b,c) vertical sections through the inner model region displaying data gradients for a homogeneous start model of 10, 000 Ωm at 100 Hz. The location of the conductive anomaly is outlined in white. Panel (c) depicts the 2D cut along the dashed line marked 'diag' in (a).

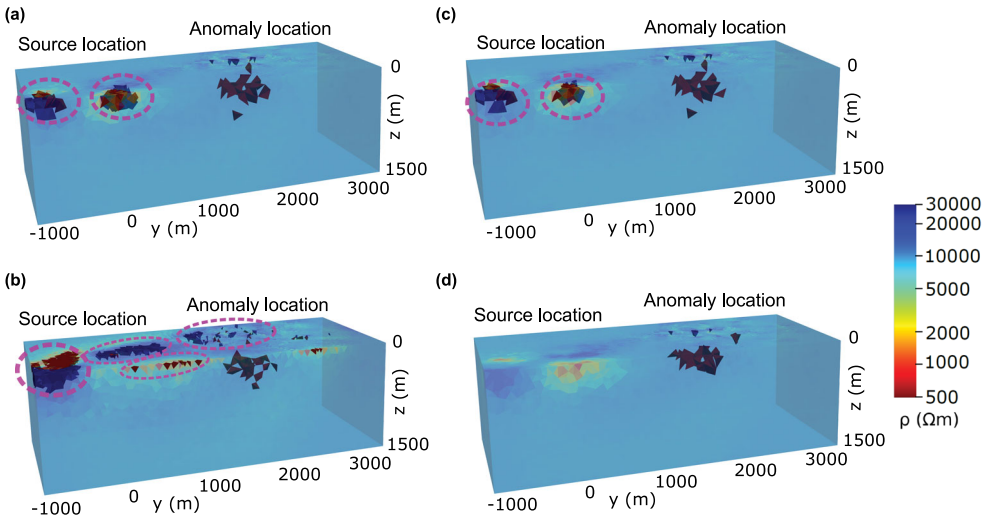

FIGURE 5 Synthetic example: 3D views of resistivity models obtained after 30 iterations for the inversion runs with (a) gradient approximation smoothing, (b) gradient approximation smoothing and Jacobi diagonal scaling for the start preconditioner (cf. Equation 7), (c) gradient approximation smoothing with distance-to-source weighting ($a = 3$, $r_d = 750$ m, cf. Equation 8) and (d) gradient approximation smoothing with distance-to-source weighting ($a = 6$, $r_d = 750$ m, cf. Equation 8). Resistivity thresholds of 500 Ωm and 25,000 Ωm visualise the most conductive and most resistive model parameters, respectively. The conductive anomaly is clearly visible in all models. The models in (a)–(c) include artefacts of extremely high and low resistivities in the vicinity of the source (encircled in pink), which is due to elevated sensitivity levels in the vicinity of the source combined with polarity changes in the gradients at the electrodes of the source bipoles (cf. Figure 4).

Distance-to-source weighting (c) and (d): The distance-to-source weighting has two input parameters (r_d and a) that can be customized by the user. A meaningful distance threshold r_d mainly depends on the distance between the source and anomalous regions in the model. We test different values for r_d and a (cf. Figure 1) and evaluate the results by investigating the inversion models (Figure 5a,c,d) and performances. A combination of $r_d = 750$ m (half of the source-anomaly

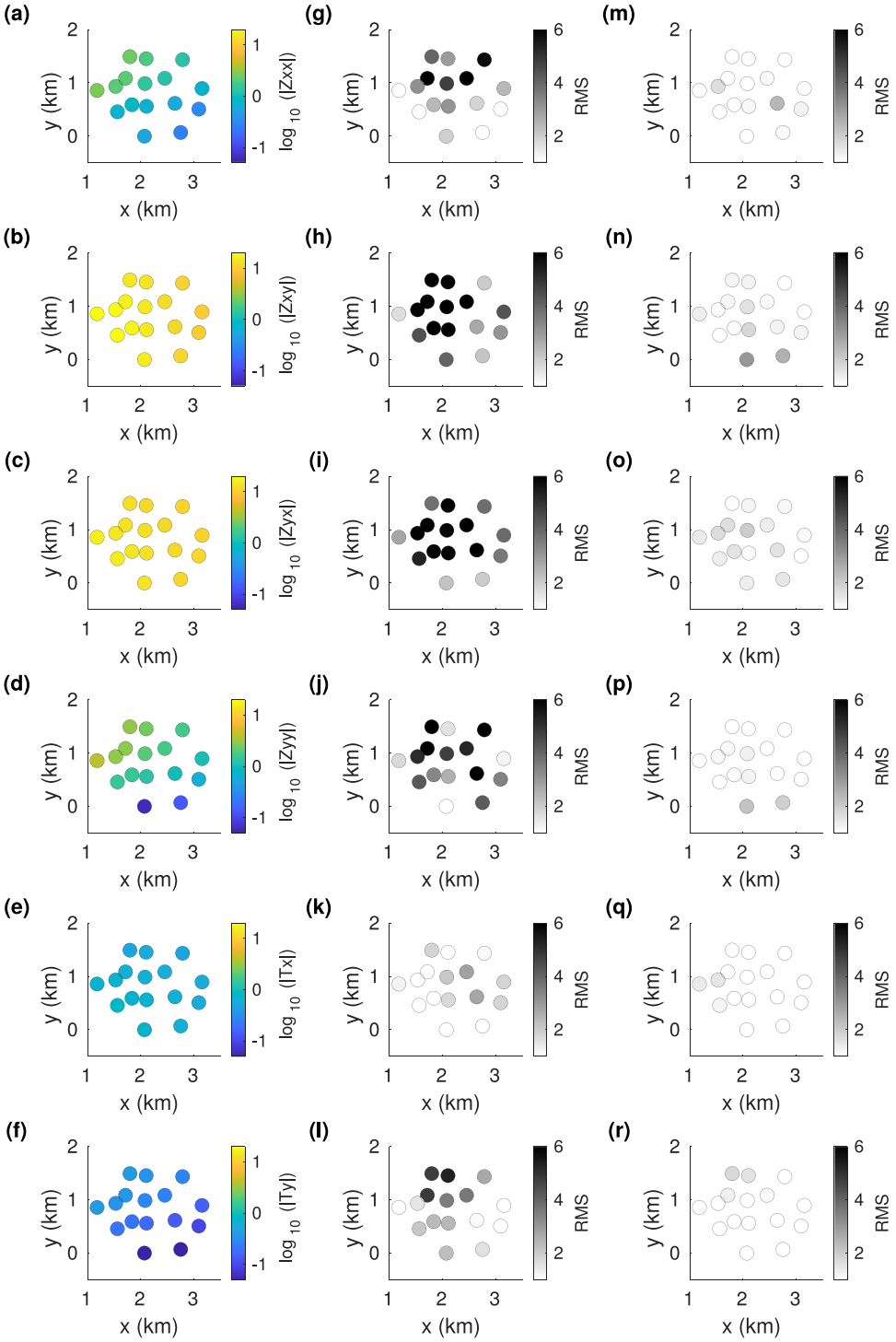

FIGURE 6 Synthetic example: Data and RMS misfits at each station. (a)–(f) Amplitudes of the input data at 100 Hz, corresponding RMS values averaged over all frequencies for (g)–(l) the start model and (m)–(r) the final resistivity model (Figures 5d and 7) obtained with distance-to-source weighting ($a = 6$, $r_d = 750$ m) in the regularization term.

distance) and $a = 6$, corresponding to inversion test (d), is identified as an appropriate parameter combination for this model for three reasons: First, highly elevated gradient levels in the immediate vicinity of the source have decayed at approximately 750 m distance from the source (cf. Figure 4a). Second, $a = 6$ results in sufficiently increased smoothing in the source region such that resistivity artefacts in the source region are reduced to a large extent (Figure 5d). Last, this parameter combination reduces inversion runtimes, as it improves the determination of favourable search directions. For comparison, inversion test (c) with a parameter combination of $r_d = 750$ m and $a = 3$ is restarted with the steepest

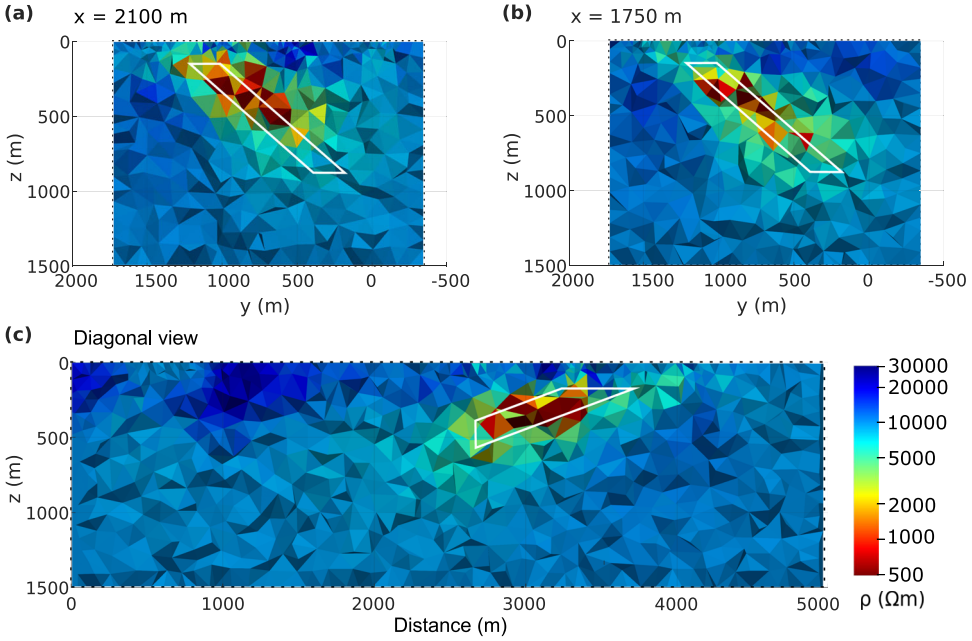

FIGURE 7 Synthetic example: Vertical sections through the inversion result after 30 iterations obtained with gradient approximation smoothing and distance-to-source weighting ($a = 6$, $r_d = 750$ m, cf. Figure 5d) in the model regularization term. A homogeneous 10,000 Ωm start model is used. Panel (c) depicts the 2D cut along the dashed line marked 'diag' in Figure 2a. The true location of the resistivity anomaly is outlined in white.

descend search directions in 27 out of 30 iterations and therefore requires approximately 1.5 times as much time as the inversion test (d). In the latter, better search directions than the steepest descent are found in 22 out of 30 iterations, meaning there were only eight iterations with restarts.

Convergence and data fit

All inversion runs converge from an average total RMS value of 7.8 for the start model towards an average total RMS value of 1.1. Input data, responses of the start model and the final model (cf. Figure 5d) resulting from the inversion run with distance-to-source weighting ($a = 6$, $r_d = 750$ m) applied are shown exemplarily for four stations in Figure 3. Average RMS values per station of the final model indicate an overall good data fit (Figure 6).

Resistivity model

Figure 7 shows vertical sections through the resistivity model obtained after 30 iterations for the inversion run with gradient approximation smoothing combined with distance-to-source weighting ($a = 6$, $r_d = 750$ m, cf. Figure 5d). The location and extent of the inclined conductive anomaly are clearly visible and its true resistivity is well recovered at its centre. With the distance-to-source weighting applied, we aim at counteracting the high sensitivities close to the source (Figure 4) by increasing the smoothing in the source region. The weighting largely reduces the resistivity contrasts in the source region so that the most prominent feature in the model is actually the target. Similar to Avdeev and Avdeeva (2009) in their magnetotellurics (MT) models with sparse station coverage, small-scale resistive artefacts are visible close to the receiver locations that are a result of the high sensitivity values at the receiver sites (Figure 4).

APPLICATION TO FIELD DATA

Controlled-source electromagnetics (CSEM) data collected on a frozen lake in Stockholm, Sweden, are selected to demonstrate the inversion of a field data set (Figure 8). The main purpose of acquiring CSEM data was to increase the depth penetration compared to previously measured radiomagnetotellurics (RMT) data (Bastani et al., 2015; Mehta et al., 2017). Parts of the CSEM data have been evaluated together with the RMT data in a 2D far-field inversion approach (Bastani et al., 2022) to investigate the depth to bedrock and study the possible presence of fracture systems crossing a planned by-pass tunnel below the lake, which is part of an infrastructure project. However, data with near-field signatures had to be excluded from this inversion approach. Here, the developed 3D CSEM inversion code is applied to all collected CSEM data.

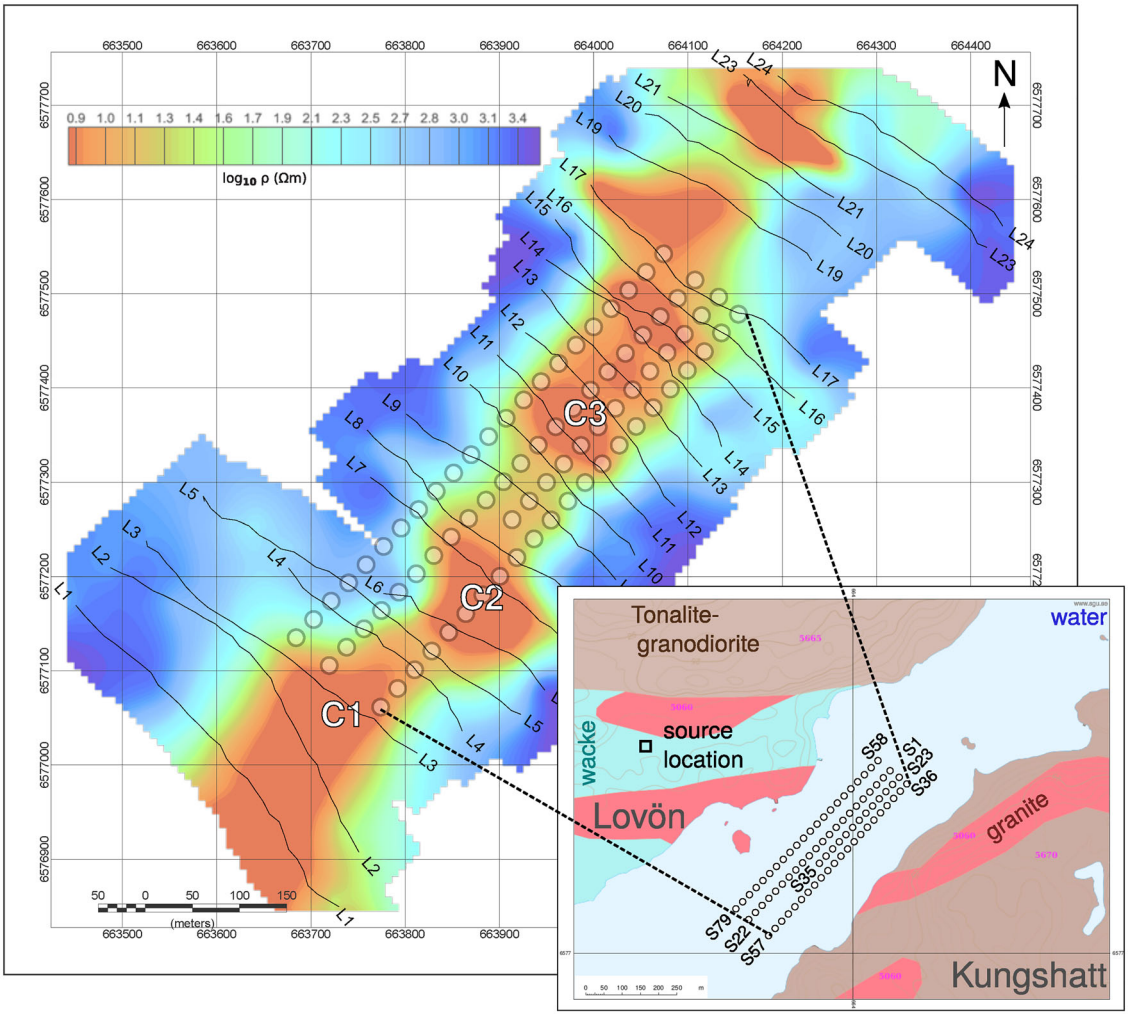

FIGURE 8 Field example: Map with CSEM receiver stations (white circles) combined with the gridded resistivity at 38 m depth using the resistivity models from 2D inversion of determinant RMT data along 24 profiles (black lines) presented in Mehta et al. (2017). Prominent conductive features are labelled with C1, C2 and C3. Start and end-points of each CSEM receiver line are labelled with their station numbers in the inset figure (geological map obtained from SGU (2023)). The location of the CSEM source with respect to the station locations is also shown on top of the inset map.

The data set was collected with the EnviroMT system (Bastani, 2001). It consists of 79 stations placed at 25 m intervals along four profiles (Figure 8). Electric fields were recorded with electrodes that were in direct contact with the lake water. Magnetic fields were obtained with a three-component magnetometer on top of the frozen lake. A horizontal double magnetic dipole transmitter was located on land at a distance of 477 m to a maximum of 625 m to the receiver grid. The transmitter is modelled with two pairs of vertical closed loops perpendicular to the magnetic dipole directions.

The data were processed, and data uncertainties were obtained as described by Bastani et al. (2022). These are then used for the inversion. Distinct outliers are manually identified and down-weighted by increasing their uncertainties. Off-diagonal impedance tensor components at five frequencies, 2.5, 3.2, 5.0, 8.0 and 10 kHz, are selected as input data for the inversion. Diagonal impedance tensor components are not used, as they cluster around zero and, thus, are not expected to hold much information on the subsurface. The uncertainties of the 8.0 and 10 kHz data are doubled, as the data quality is worse compared to the lower frequency data, that is the data show higher variability and larger uncertainties, presumably because of source instability at higher frequencies.

The upper parts of the 2D models obtained by the inversion of Transverse-electric (TE-) and Transverse-magnetic (TM)-mode RMT data in the frequency range of 14–250 kHz (Bastani et al., 2022) are used to construct a 3D start model (Figure 9a) for 3D CSEM inversion: The water column is modelled with a resistivity of 300 Ωm down to a depth of 10 m. Below the water column, a sediment layer of 100 Ωm down to a depth of 20 m is included. The sediment layer has probably lower resistivities (approximately

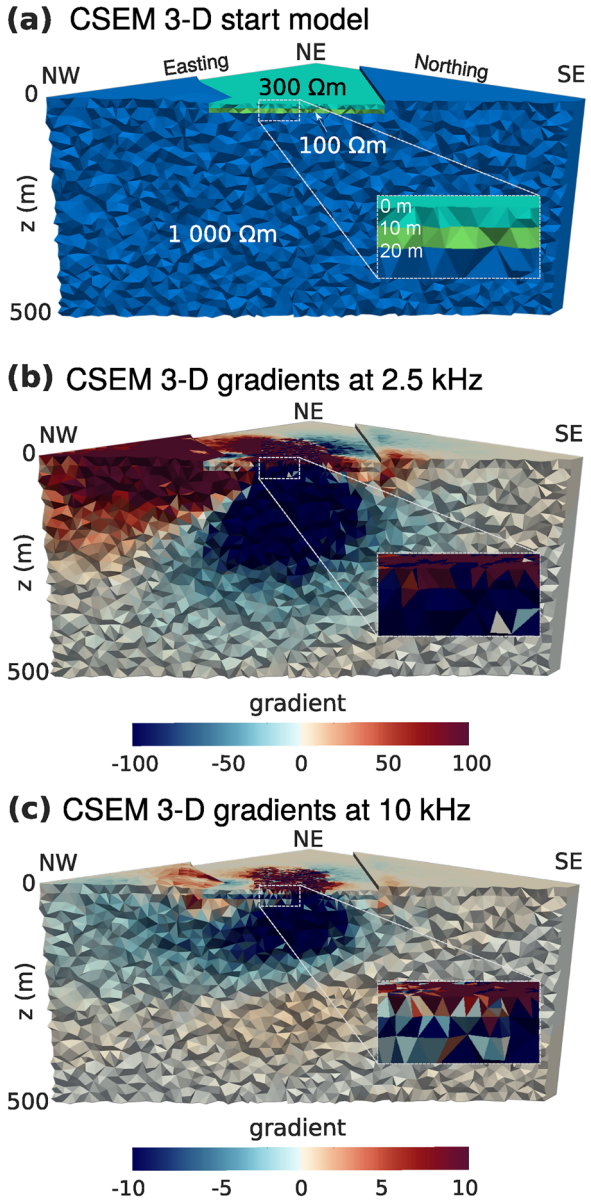

FIGURE 9 Field example: Vertical sections along RMT profile L9 (cf. Figure 8) through the inner model region of the 3D CSEM (a) start model and (b, c) data gradients w.r.t. the start model at 2.5 and 10 kHz. The crinkle clip (clip without cutting through elements) illustrates the tetrahedral mesh of the model. The magnetic source is located in the north-western part of the model. The lake water and underlying sediments are included in the start model, as 10 m thick layers of 300 and 100 Ωm, respectively. Receiver lines are located on top of the water. Data gradients indicate strong positive values (red) towards the source direction at 2.5 kHz and small negative values (light blue) at 10 kHz. Strong negative values (blue) below the receiver profiles suggest a conductive anomaly below the water. The lengths of the horizontal axes (Northing and Easting) are the same as in Figure 11.

30 Ωm; Mehta et al., 2017), but the inversion process may decrease the resistivities in those cells of the sediment layer the CSEM data are sensitive to. In the remaining part of the free model region that spans a volume covering the area of interest including source and receivers to a depth of 700 m and in the outer padding cells, the start model is set to 1000 Ωm, representing an estimated average resistivity of the bedrock. Along the shorelines, an approximation of the bedrock topography is included in the model. The overall domain size amounts to 100×100×100 km^3 and the inner model domain consists of 339,220 free model parameters that can be changed during inversion.

Field data sensitivities

For the start model, data gradients (cf. Section Sensitivities) at the lowest measured frequency of 2.5 kHz (Figure 9b) show strong sensitivities in the NW part of the model, that is the source vicinity, expanding towards the central model region below the receiver profiles and beyond, whereas the sensitivities of the highest frequency of 10 kHz (Figure 9b) are focused mainly below the receiver profiles. Strong negative data gradients below the receiver profiles down to a depth of ca. 300 m indicate the presence of a conductive anomaly in this region. In the water and sediment layers included in the start model (0–20 m depth), high gradient amplitudes are only observed directly below the receiver stations indicating a lack of sensitivity to these upper layers at lateral distance from the receivers.

Convergence and data fit

The inversion runs are performed with absolute differences in regularization and distance-to-source weights with a threshold $r_d = 200$ m and an exponent $a = 6$ (Equation 8). As in the synthetic example (cf. Section Synthetic Data Example), we choose parameter r_d such that it corresponds to approximately half of the source–receiver distance while taking into account that the shoreline is located at a distance of ca. 200 m from the source. The inversion is restarted several times with decreased regularization parameters to facilitate a better data fit. Within 125 iterations, the inversion reduces the total average root mean square error (RMS) from 190 for the start model to 2.3 for the final model. The data including uncertainties and model responses are presented in Figure 10. The lower frequency data are of rather good quality and well fitted. The

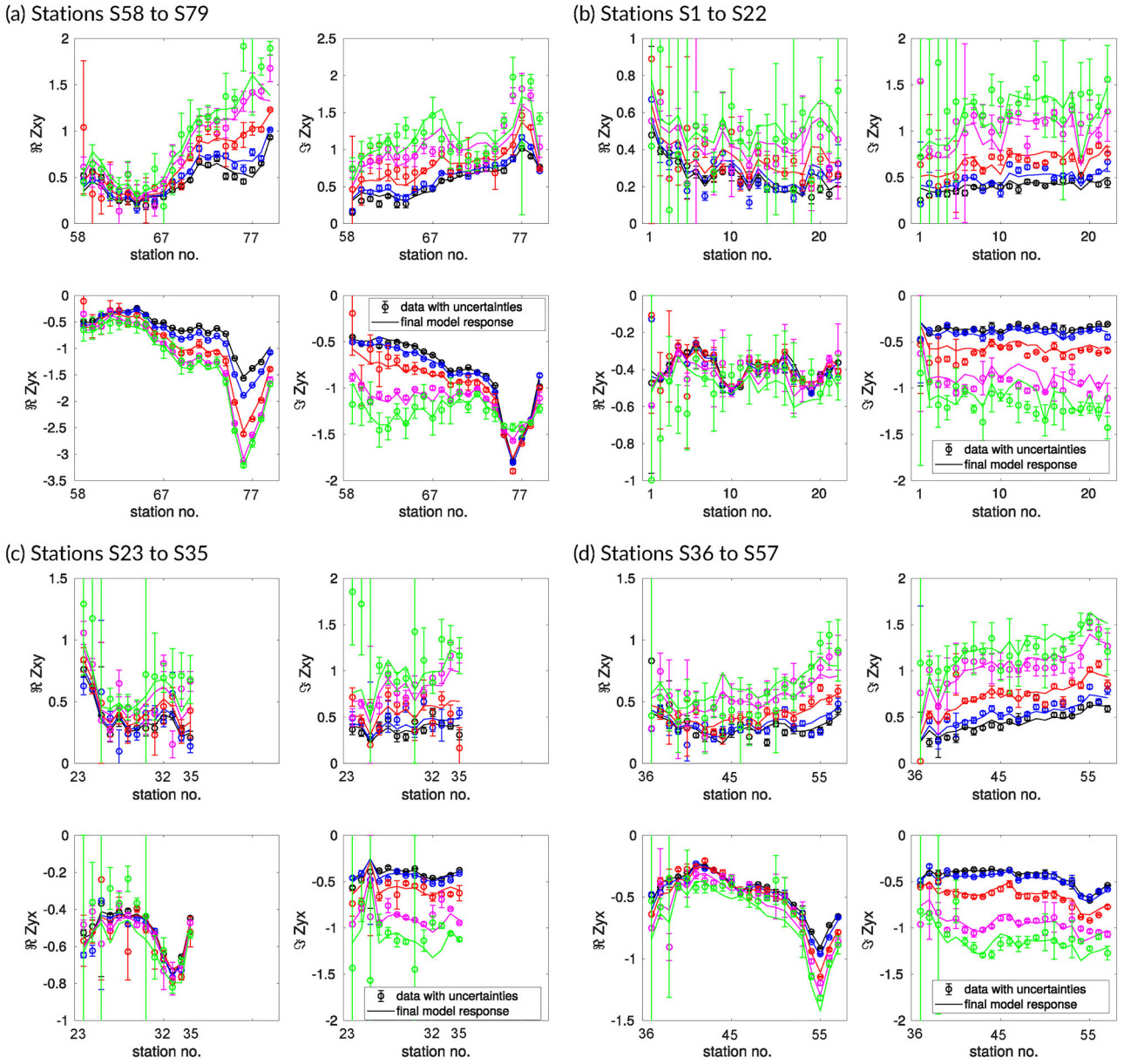

FIGURE 10 Field example: Field data with uncertainties and responses of the 3D inversion model displayed in Figure 11 for the real (ℝ) and imaginary (𝕀) parts of the off-diagonal impedances of the four CSEM profiles (see Figure 8). Average RMS: 2.3. Different colours indicate different frequencies: 2.5 kHz (black), 3.2 kHz (blue), 5.0 kHz (red), 8.0 kHz (magenta) and 10 kHz (green).

data points of the two highest frequencies show high variability and are, because of their increased uncertainty levels, partly poorly fitted. Another reason for the poor data fit at the higher frequencies might be that the mesh is not sufficiently fine. For comparison, the tetrahedral cells of the 3D model are approximately three to four times larger in diameter than the rectangular cells in the previously computed 2D models. However, the size of this 3D inversion problem is close to the maximum that `emilia` can currently handle in reasonable run times on the computer platform at our disposal (one node of 256 GB memory consisting of two Intel Xeon E5 2630 v4 processors at 2.20 GHz/core on the *Rackham* cluster belonging to the National Academic Infrastructure for Supercomputing in Sweden).

Resistivity models

Figure 11 displays depth slices at 38 and 57 m through the obtained 3D resistivity model. Suppressed by the distance-to-source weighting, only a very limited source signature is visible in the source region, and it does not expand towards the area of interest below the receiver profiles. The bedrock resistivity in the 3D CSEM model along the NW shoreline

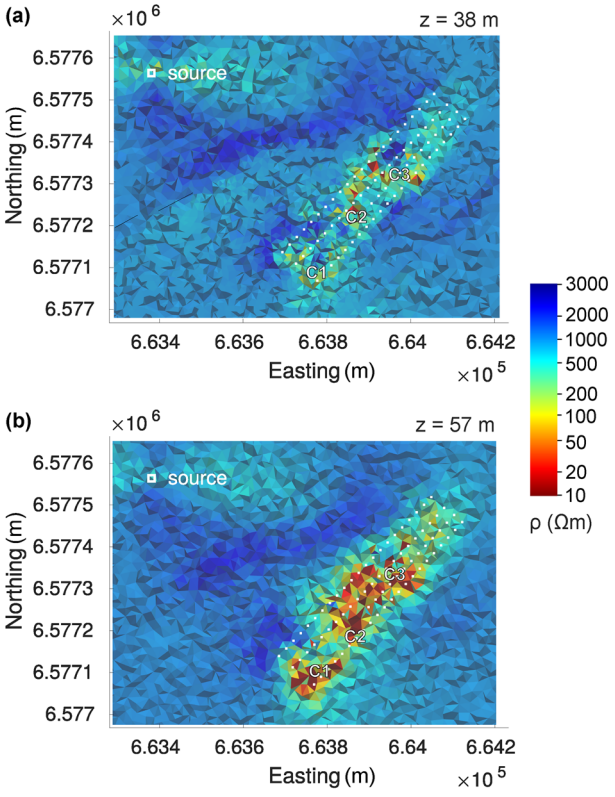

FIGURE 11 Field example: Depth slices at (a) 38 m and (b) 57 m through the 3D resistivity model obtained from inversion of CSEM impedance data. Source and receiver positions are depicted with white symbols. Prominent conductive anomalies (C1, C2, C3) can be observed at the same lateral locations as in the 2D models obtained from the RMT data (Figure 8).

is increased from the 1000 Ωm value of the start model, which is also observed in the RMT model (Figure 8). As compared to the start model, model parameters are changed the most below the receiver profiles in regions of high sensitivity (cf. Figure 9). Comparing the depth slices through the 3D CSEM model (Figure 11) to the RMT model produced by determinant inversion (Figure 8), similar conductive features (C1–C3) can be identified, but, in the 3D CSEM model, they are more pronounced at greater depth (Figure 11b). This observation fits the statement of Bastani et al. (2022) that the CSEM data are able to resolve deeper conductive structures. These conductors are suspected to be a signature of fractured bedrock filled with conductive minerals and clays (Bastani et al., 2022).

Moreover, in the 3D CSEM inversion, the inclusion of some of the lower frequency data excluded by Bastani et al. (2022) results in better depth penetration which in turn provides better control on possible low-resistivity fractures within the crystalline bedrock. Comparing the depth slices in Figures 11a and 11b reveals that the low-resistivity features continue below 38 m depth along almost all profiles and coincide well with the fracture zones suggested on geological maps (Bastani et al., 2022). Note that the 3D tetrahedral mesh is too coarse to adequately image small-scale features and to lead to a detailed comparison of the 2D and 3D models (cf. Section Convergence and Data Fit for information on computer platform limitations). We expect, that smaller cells in the inner model region would result in a smoother resistivity model in the depth range, where the conductive anomalies are located.

DISCUSSION AND CONCLUSIONS

We have presented successful applications of a preconditioned non-linear conjugate gradient (NLCG) inverse algorithm complemented with new modules for 3D data handling, gradient computations and regularization to produce 3D resistivity models from controlled-source electromagnetic (CSEM) impedance tensor and vertical magnetic transfer functions (VMTF) data. Land-based 3D CSEM inversion can suffer from heterogeneous sensitivities due to a limited number of or not optimally deployed sources and receiver stations. Having a preconditioned NLCG inversion algorithm at hand, we investigated its capabilities for CSEM inversion. The results reveal that it produces reliable resistivity models, even for models with a single source location. However, we suggest to counteract the footprint of the source with a customized distance weighting functional in the regularization term.

The presented synthetic example demonstrates, that the NLCG approach can be used to invert land-based CSEM data. However, future investigations and developments are necessary to improve the inversion approach and its performance. For instance, we obtain very rough models in the vicinity of the receivers, which can be a result of jumps in the data gradients across the small cells at the receiver locations. This could be counteracted with an additional regularization based on smoothing the model gradients in the shallower part of the model. Another option to obtain overall smoother, more consistent models is to implement a dual mesh approach, where forward modelling and inversion parameter meshes differ. The inversion mesh can then consist of larger, more uniformly shaped cells than in the forward modelling mesh, which results in a better determined inversion problem. It would also make fixing the near-surface layer less necessary. To make the presented code competitive, its performance has to be improved. Therefore, it is planned to work on its parallelization and on implementing iterative solution methods for solving the forward and pseudo-forward problems. Additionally, higher order interpolation functions and adaptive mesh refinement could be used to reduce the number of model parameters and, at the same time, obtain better accuracy of the forward responses.

The described application of the 3D inversion code to the CSEM data collected on the frozen lake produced a reasonable fit to the data and models that show a similar resistivity

distribution as those from 2D inversions of the combined radio-magnetotellurics (RMT) and CSEM data. Moreover, the inclusion of the data at the two lowest frequencies in the inversion provided sensitivity at greater depth. To improve the 3D model, all RMT and CSEM data should be combined in a joint inversion approach and a finer mesh should be used. Moreover, to rule out possible effects imposed by the single source location in the resistivity model, one can conduct similar measurements with a new source location and study the similarities and differences between the 3D resistivity models in the future.

ACKNOWLEDGEMENTS

The code development has been financed by the Smart Exploration project (European Union's Horizon 2020 funding under grant agreement No. 775971). The computations were enabled by resources provided by the National Academic Infrastructure for Supercomputing in Sweden (NAISS) at UPPMAX (Dnr: SNIC 2022/5-530) partially funded by the Swedish Research Council through grant agreement no. 2022-06725.

DATA AVAILABILITY STATEMENT

The mesh files and synthetic data that were produced for this work and support the findings of this study are available from the corresponding author upon reasonable request. All sufficiently tested parts of the software `emilia` are available on a peer-to-peer basis for scientific purposes from Thomas Kalscheuer.

ORCID

Paula Rulff https://orcid.org/0000-0001-6714-8008
Thomas Kalscheuer https://orcid.org/0000-0003-3819-8182
Mehrdad Bastani https://orcid.org/0000-0003-3564-3754
Dominik Zbinden https://orcid.org/0000-0003-4540-4386

REFERENCES

Abubakar, A., Habashy, T.M., Li, M. & Liu, J. (2009) Inversion algorithms for large-scale geophysical electromagnetic measurements. *Inverse Problems*, 25(12), 123012.

Amaya, M. (2015) High-order optimization methods for large-scale 3D CSEM data inversion. PhD thesis, Norwegian University of Science and Technology, Trondheim, Norway.

Amestoy, P., Brossier, R., Buttari, A., L'Excellent, J.-Y., Mary, T., Métivier, L., Miniussi, A. & Operto, S. (2016) Fast 3D frequency-domain full-waveform inversion with a parallel block low-rank multifrontal direct solver: application to OBC data from the North Sea. *Geophysics*, 81(6), R363–R383.

Avdeev, D. & Avdeeva, A. (2009) 3D magnetotelluric inversion using a limited-memory quasi-Newton optimization. *Geophysics*, 74(3), F45–F57.

Bastani, M. (2001) EnviroMT - A new controlled source/radio magnetotelluric system. PhD thesis, Uppsala University, Uppsala, Sweden.

Bastani, M., Johansson, H., Paulusson, A., Paulusson, K. & Dynesius, L. (2020) Unmanned aerial vehicles (UAV) and ground-based electromagnetic (EM) systems. *First Break*, 38(8), 87–89.

Bastani, M., Persson, L., Mehta, S. & Malehmir, A. (2015) Boat-towed radio-magnetotellurics - a new technique and case study from the city of Stockholm. *Geophysics*, 80(6), B193–B202.

Bastani, M., Sadeghi, M. & Malehmir, A. (2019) 3D magnetic susceptibility model of a deep iron-oxide apatite-bearing orebody incorporating borehole data in Blötberget. Paper presented at the 16th SAGA Biennial Conference & Exhibition 2019.

Bastani, M., Wang, S., Malehmir, A. & Mehta, S. (2022) Radio-magnetotelluric and controlled-source magnetotelluric surveys on a frozen lake: Opportunities for urban applications in Nordic countries. *Near Surface Geophysics*, 20(1), 30–45.

Bretaudeau, F. & Coppo, N. (2016) A pseudo-MT formulation for 3D CSEM inversion with a single transmitter. Paper presented at the Electromagnetic Induction Workshop, August 2016 (EMIW2016), Chiang Mai, Thailand.

Cai, H., Long, Z., Lin, W., Li, J., Lin, P. & Hu, X. (2021) 3D multinary inversion of controlled-source electromagnetic data based on the finite-element method with unstructured mesh. *Geophysics*, 86(1), E77–E92.

Cao, M., Tan, H.D. & Wang, K.P. (2016) 3D LBFGS inversion of controlled source extremely low frequency electromagnetic data. *Applied Geophysics*, 13(4), 689–700.

Castillo-Reyes, O., Queralt, P., Marcuello, A. & Ledo, J. (2021) Land CSEM simulations and experimental test using metallic casing in a geothermal exploration context: Vallés basin (NE Spain) case study. *IEEE Transactions on Geoscience and Remote Sensing*, 60, 1–13.

Commer, M. & Newman, G.A. (2008) New advances in three-dimensional controlled-source electromagnetic inversion. *Geophysical Journal International*, 172(2), 513–535.

Fletcher, R. & Reeves, C.M. (1964) Function minimization by conjugate gradients. *The Computer Journal*, 7(2), 149–154.

Grayver, A.V., Streich, R. & Ritter, O. (2013) Three-dimensional parallel distributed inversion of CSEM data using a direct forward solver. *Geophysical Journal International*, 193(3), 1432–1446.

Grayver, A.V., Streich, R. & Ritter, O. (2014) 3D inversion and resolution analysis of land-based CSEM data from the Ketzin CO_2 storage formation. *Geophysics*, 79(2), E101–E114.

Gribenko, A. & Zhdanov, M. (2007) Rigorous 3D inversion of marine CSEM data based on the integral equation method. *Geophysics*, 72(2), WA73–WA84.

Günther, T., Rücker, C. & Spitzer, K. (2006) Three-dimensional modelling and inversion of dc resistivity data incorporating topography - II. Inversion. *Geophysical Journal International*, 166(2), 506–517.

Haber, E., Ascher, U.M. & Oldenburg, D.W. (2004) Inversion of 3D electromagnetic data in frequency and time domain using an inexact all-at-once approach. *Geophysics*, 69(5), 1216–1228.

Heagy, L.J., Cockett, R., Kang, S., Rosenkjaer, G.K. & Oldenburg, D.W. (2017) A framework for simulation and inversion in electromagnetics. *Computers and Geosciences*, 107(June), 1–19.

Hördt, A. & Scholl, C. (2004) The effect of local distortions on time-domain electromagnetic measurements. *Geophysics*, 69(1), 87–96.

Hunkeler, P.A., Hendricks, S., Hoppmann, M., Farquharson, C.G., Kalscheuer, T., Grab, M., Kaufmann, M.S., Rabenstein, L. & Gerdes, R. (2016) Improved 1D inversions for sea ice thickness and conductivity from electromagnetic induction data: inclusion of nonlinearities caused by passive bucking. *Geophysics*, 81(1), WA45–WA58.

Hunkeler, P.A., Hoppmann, M., Hendricks, S., Kalscheuer, T. & Gerdes, R. (2016) A glimpse beneath Antarctic sea ice: platelet layer volume from multifrequency electromagnetic induction sounding. *Geophysical Research Letters*, 43(1), 222–231.

Kalscheuer, T., Blake, S., Podgorski, J.E., Wagner, F., Green, A.G., Muller, M., Jones, A.G., Maurer, H., Ntibinyane, O. & Tshoso, G. (2015) Joint inversions of three types of electromagnetic data explicitly constrained by seismic observations: results from the central Okavango Delta, Botswana. *Geophysical Journal International*, 202(3), 1429–1452.

Kalscheuer, T., Garcia Juanatey, M., Meqbel, N. & Pedersen, L.B. (2010) Non-linear model error and resolution properties from two-dimensional single and joint inversions of direct current resistivity and radiomagnetotelluric data. *Geophysical Journal International*, 182(3), 1174–1188.

Kalscheuer, T., Hübert, J., Kuvshinov, A., Lochbühler, T. & Pedersen, L.B. (2012) A hybrid regularization scheme for the inversion of magnetotelluric data from natural and controlled sources to layer and distortion parameters. *Geophysics*, 77(4), E301–E315.

Kalscheuer, T., Juhojuntti, N. & Vaittinen, K. (2018) Two-dimensional magnetotelluric modelling of ore deposits: improvements in model constraints by inclusion of borehole measurements. *Surveys in Geophysics*, 39(3), 467–507.

Kalscheuer, T. & Pedersen, L.B. (2007) A non-linear truncated SVD variance and resolution analysis of two-dimensional magnetotelluric models. *Geophysical Journal International*, 169(2), 435–447.

Kalscheuer, T., Pedersen, L.B. & Siripunvaraporn, W. (2008) Radiomagnetotelluric two-dimensional forward and inverse modelling accounting for displacement currents. *Geophysical Journal International*, 175(2), 486–514.

Kamm, J., Lundin, I.A., Bastani, M., Sadeghi, M. & Pedersen, L.B. (2015) Joint inversion of gravity, magnetic, and petrophysical data - A case study from a gabbro intrusion in Boden, Sweden. *Geophysics*, 80(5), B131–B152.

Kara, K.B. & Farquharson, C.G. (2023) 3D minimum-structure inversion of controlled-source EM data using unstructured grids. *Journal of Applied Geophysics*, 209, 104897.

Kelbert, A., Meqbel, N., Egbert, G.D. & Tandon, K. (2014) ModEM: a modular system for inversion of electromagnetic geophysical data. *Computers and Geosciences*, 66, 40–53.

Key, K. (2016) MARE2DEM: A 2-D inversion code for controlled-source electromagnetic and magnetotelluric data. *Geophysical Journal International*, 207(1), 571–588.

Kim, H.J. & Kim, Y. (2011) A unified transformation function for lower and upper bounding constraints on model parameters in electrical and electromagnetic inversion. *Journal of Geophysics and Engineering*, 8(1), 21–26.

Li, X. & Pedersen, L.B. (1991) Controlled source tensor magnetotellurics. *Geophysics*, 56(9), 1456–1461.

Li, Y. & Oldenburg, D.W. (1996) 3-D inversion of magnetic data. *Geophysics*, 61(2), 394–408.

Long, Z., Cai, H., Hu, X., Li, G. & Shao, O. (2020) Parallelized 3-D CSEM Inversion with Secondary Field Formulation and Hexahedral Mesh. *IEEE Transactions on Geoscience and Remote Sensing*, 58(10), 6812–6822.

Mackie, R., Watts, M. & Rodi, W. (2007) Joint 3D inversion of marine CSEM and MT data. In *SEG technical program expanded abstracts 2007*. Houston, TX: Society of Exploration Geophysicists, pp. 574–578.

Malehmir, A., Maries, G., Bäckström, E., Schön, M. & Marsden, P. (2017) Developing cost-effective seismic mineral exploration methods using a landstreamer and a drophammer. *Scientific Reports*, 7(1), 1–7.

Maries, G., Malehmir, A., Bäckström, E., Schön, M. & Marsden, P. (2017) Downhole physical property logging for iron-oxide exploration, rock quality, and mining: an example from central Sweden. *Ore Geology Reviews*, 90(October), 1–13.

Markovic, M., Maries, G., Malehmir, A., von Ketelhodt, J., Bäckström, E., Schön, M. & Marsden, P. (2020) Deep reflection seismic imaging of iron-oxide deposits in the Ludvika mining area of central Sweden. *Geophysical Prospecting*, 68(1), 7–23.

McGillivray, P.R. & Oldenburg, D.W. (1990) Methods for calculating Fréchet derivatives and sensitivities for the non-linear inverse problem: a comparative study. *Geophysical Prospecting*, 38(5), 499–524.

Mehta, S., Bastani, M., Malehmir, A. & Pedersen, L.B. (2017) Resolution and sensitivity of boat-towed RMT data to delineate fracture zones - example of the Stockholm bypass multi-lane tunnel. *Journal of Applied Geophysics*, 139, 131–143.

Newman, G.A. & Alumbaugh, D.L. (2000) Three-dimensional magnetotelluric inversion using non-linear conjugate gradients. *Geophysical Journal International*, 140(2), 410–424.

Newman, G.A. & Boggs, P.T. (2004) Solution accelerators for large-scale three-dimensional electromagnetic inverse problems. *Inverse Problems*, 20(6), S151–S170.

Newman, G.A. & Commer, M. (2008) New advances in three-dimensional controlled-source electromagnetic inversion. *Geophysical Journal International*, 172(2), 513–535.

Nocedal, J. & Wright, S. (2006) *Numerical optimization*, second edition. Berlin: Springer.

Pedersen, L.B. (1982) The magnetotelluric impedance tensor - its random and bias errors. *Geophysical Prospecting*, 30(2), 188–210.

Pedersen, L.B., Bastani, M. & Dynesius, L. (2005) Groundwater exploration using combined controlled-source and radiomagnetotelluric techniques. *Geophysics*, 70(1), 8–15.

Pedersen, L.B. & Engels, M. (2005) Routine 2D inversion of magnetotelluric data using the determinant of the impedance tensor. *Geophysics*, 70(2), G33–G41.

Plessix, R.E. & Mulder, W.A. (2008) Resistivity imaging with controlled-source electromagnetic data: depth and data weighting. *IOP Science Inverse Problems*, 24(3), 034012.

Polak, E. & Ribiere, G. (1969) Note sur la convergence de méthodes de directions conjuguées. *Revue française d'informatique et de recherche opérationnelle. Série rouge*, 3(R1), 35–43.

Rochlitz, R., Becken, M. & Günther, T. (2023) Three-dimensional inversion of semi-airborne electromagnetic data with a second-order finite-element forward solver. *Geophysical Journal International*, 234(1), 528–545.

Rücker, C. (2011) Advanced electrical resistivity modelling and inversion using unstructured discretization. PhD thesis, University of Leipzig, Leipzig, Germany.

Rulff, P. (2023) Three-dimensional forward modelling and inversion of controlled-source electromagnetic data using the edge-based finite-element method. PhD thesis, Uppsala University, Uppsala, Sweden.

Rulff, P., Buntin, L.M. & Kalscheuer, T. (2021) Efficient goal-oriented mesh refinement in 3-D finite-element modelling adapted for controlled source electromagnetic surveys. *Geophysical Journal International*, 227(3), 1624–1645.

Rulff, P. & Kalscheuer, T. (2024) A comparison between normalised controlled-source electromagnetic field components and transfer functions as input data for three-dimensional non-linear conjugate gradient inversion. *Geophysical Prospecting*, 72(5), 2005–2012.

Sasaki, Y., Yi, M.J., Choi, J. & Son, J.S. (2015) Frequency and time domain three-dimensional inversion of electromagnetic data for a grounded-wire source. *Journal of Applied Geophysics*, 112, 106–114.

Schaller, A., Streich, R., Drijkoningen, G., Ritter, O. & Slob, E. (2018) A land-based controlled-source electromagnetic method for oil field exploration: an example from the Schoonebeek oil field. *Geophysics*, 83(2), WB1–WB17.

SGU (2023) SGUs kartvisare. Accessed: 2023-09-30. https://apps.sgu.se/kartvisare/kartvisare-berggrund-1-miljon.html.

Shewchuk, J.R. (1994) An introduction to the conjugate gradient method without the agonizing pain. Technical report, Carnegie Mellon University, USA.

Si, H. (2015) TetGen, a delaunay-based quality tetrahedral mesh generator. *ACM Transactions on Mathematical Software*, 41(2), 1–36.

Smirnova, M., Shlykov, A., Asghari, S.F., Tezkan, B., Saraev, A., Yogeshwar, P. & Smirnov, M. (2023) 3D controlled-source electromagnetic inversion in the radio-frequency band. *Geophysics*, 88(1), E1–E12.

Soyer, W. & Brasse, H. (2001) A magneto-variation array study in the central Andes of N Chile and SW Bolivia. *Geophysical Research Letters*, 28(15), 3023–3026.

Streich, R. (2016) Controlled-source electromagnetic approaches for hydrocarbon exploration and monitoring on land. *Surveys in Geophysics*, 37(1), 47–80.

Tietze, K., Ritter, O., Patzer, C., Veeken, P. & Dillen, M. (2019) Repeatability of land-based controlled-source electromagnetic measurements in industrialized areas and including vertical electric fields. *Geophysical Journal International*, 218(3), 1552–1571.

Tikhonov, A.N. & Arsenin, V.I.V.I. (1977) *Solutions of ill-posed problems*. Scripta series in mathematics. Washington: Winston.

Wang, S., Kalscheuer, T., Bastani, M., Malehmir, A., Pedersen, L.B., Dahlin, T. & Meqbel, N. (2018) Joint inversion of lake-floor electrical resistivity tomography and boat-towed radio-magnetotelluric data illustrated on synthetic data and an application from the Äspö Hard Rock Laboratory site, Sweden. *Geophysical Journal International*, 213(1), 511–533.

Yan, P., Garcia Juanatey, M., Kalscheuer, T., Juhlin, C., Hedin, P., Savvaidis, A., Lorenz, H. & Kück, J. (2017) A magnetotelluric investigation of the Scandinavian Caledonides in western Jämtland, Sweden, using the COSC borehole logs as prior information. *Geophysical Journal International*, 208(3), 1465–1489.

Yan, P., Kalscheuer, T., Hedin, P. & Garcia Juanatey, M. (2017) Two-dimensional magnetotelluric inversion using reflection seismic data as constraints and application in the COSC project. *Geophysical Research Letters*, 44(8), 3554–3563.

Zbinden, D. (2015) Inversion of 2D magnetotelluric and radiomagnetotelluric data with non-linear conjugate gradient techniques. Master's thesis, Uppsala University, Uppsala, Sweden.

Zhang, Y. (2015) Parallel goal-oriented adaptive finite element modeling for 3D electromagnetic exploration. PhD thesis, University of California San Diego, San Diego, CA.

Zonge, K.L. & Hughes, L.J. (1991) Controlled source audio-frequency magnetotellurics. In *Electromagnetic methods in applied geophysics: Volume 2, Application, Parts A and B*. Tulsa, OK: Society of Exploration Geophysicists, pp. 713-810.

How to cite this article: Rulff, P., Kalscheuer, T., Bastani, M. & Zbinden, D. (2024) Three-dimensional electromagnetic inversion of transfer function data from controlled sources. *Geophysical Prospecting*, 1–19. https://doi.org/10.1111/1365-2478.13660

APPENDIX A: INVERSION FRAMEWORK

The framework `emilia` (**E**lectro**m**agnetic **I**nversion with **L**east **I**ntricate **A**lgorithms, Figure A.1) is used to conduct the inversions presented in this work. `emilia` is a flexible inversion code for data from a variety of electromagnetic methods (Kalscheuer et al., 2008, 2010, 2015) written in modern FORTRAN (2018+ standard). It is based on an object-oriented approach using abstract objects for (i) field data, (ii) the computation of forward and sensitivity responses, (iii) models, (iv) model regularization, (v) model error and resolution estimates and (vi) data resolution estimates. Objects and arrays are dynamically allocated during runtime. Shared memory parallelization is performed using OpenMP and vectorization using auto-vectorization or OpenMP. To enable 3D inversion of very large models and data sets, Message Passing Interface (MPI) parallelization is planned to be implemented in the future.

3D modules for finite-element controlled-source electromagnetic (CSEM) forward and inverse modelling have been recently implemented and tested in Rulff (2023) and Rulff and Kalscheuer (2024). For two-dimensional (2D) problems, the code supports joint and single inversions of

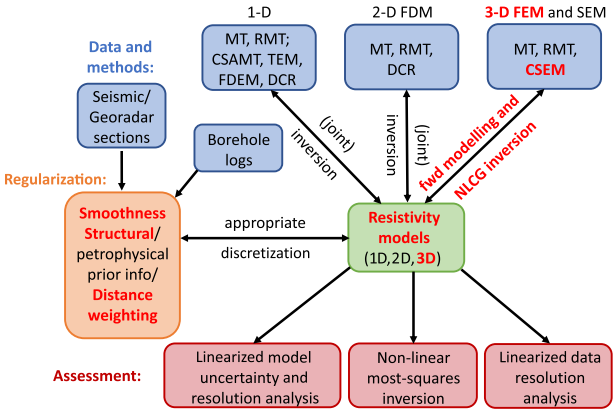

FIGURE A.1 Schematic illustration of the inversion framework `emilia`. The components reported on in this article are highlighted in bright red text. CSAMT, controlled-source audio-magnetotellurics; CSEM, controlled-source electromagnetics; DCR, direct-current resistivity; FDEM, frequency-domain electromagnetics; FDM, finite-difference method; FEM, finite-element method; RMT, radio-magnetotellurics; MT, magnetotellurics; RMT, radio-magnetotellurics; TEM, time-domain electromagnetics.

magnetotellurics (MT), audiomagnetotelluric (AMT), radiomagnetotelluric (RMT) and direct-current resistivity (DCR) data (Kalscheuer et al., 2010, 2018; Zbinden, 2015) based on finite-difference modelling and rectangular grids. The 2D MT/RMT modes invert apparent resistivities and phases of the impedance tensor as well as vertical magnetic transfer functions (VMTF) and can account for displacement currents (Kalscheuer et al., 2008). Inverting determinant impedance (Pedersen & Engels, 2005) and inter-station magnetic transfer function (e.g. Soyer & Brasse, 2001) data is also possible. For 2D inversion of MT, AMT, RMT or DCR data, topography and data collected at depth (Kalscheuer et al., 2018; Wang et al., 2018), that is on the sea floor or in boreholes, can be included. Resistivity borehole logs can be used as prior constraints (Yan, Garcia Juanatey, et al., 2017), and information from reflection seismic or georadar images can be included via smoothness constraints according to Yan, Kalscheuer, et al. (2017). For one-dimensional (1D) problems, inversion of tensorial or scalar controlled-source audiomagnetotelluric and AMT/MT data (impedance tensor, VMTF and determinant impedance) for layer and galvanic distortion parameters including magnetic and electric dipole sources and long grounded cable sources (Kalscheuer et al., 2012, 2015) is supported. Additionally, 1D inversions of loop-coil transient electromagnetic data (Kalscheuer et al., 2015), coil-coil frequency-domain electromagnetic data (Hunkeler, Hendricks, et al., 2016; Hunkeler, Hoppmann, et al., 2016), or DCR data for layer parameters can be performed.

Several inversion schemes are implemented. Among them, Gauss–Newton inversion with different weights on horizontal and vertical smoothness and optional additional Marquardt–Levenberg damping is most tested and frequently applied to 2D problems. It can also be used for the 3D CSEM inversion but is computationally expensive. Non-linear conjugate gradient inversion has been tested for 2D inversion of a set of MT, AMT and RMT transfer functions (Zbinden, 2015) and has been customized for 3D CSEM inversion as reported in this article. For 1D and 2D problems, model variance, model resolution and data resolution analyses can be obtained (Kalscheuer & Pedersen, 2007; Kalscheuer et al., 2010, 2015).